doi:10.1016/j.jmb.2011.01.049 J. Mol. Biol. (2011) 407, 556–570

Contents lists available at www.sciencedirect.com

Journal of Molecular Biology

journal homepage: http://ees.elsevier.com.jmb

Insights into Metalloregulation by M-box Riboswitch RNAs via Structural Analysis of Manganese-Bound Complexes

Arati Ramesh*, Catherine A. Wakeman and Wade C. Winkler*

Department of Biochemistry, The University of Texas Southwestern Medical Center, Dallas, TX 75390, USA

Received 24 October 2010;
received in revised form
18 January 2011;
accepted 25 January 2011
Available online
15 February 2011

Edited by J. Doudna

Keywords:
riboswitch;
magnesium–RNA interaction;
RNA folding;
RNA structure;
X-ray crystallography

The M-box riboswitch couples intracellular magnesium levels to expression of bacterial metal transport genes. Structural analyses on other riboswitch RNA classes, which typically respond to a small organic metabolite, have revealed that ligand recognition occurs through a combination of base-stacking, electrostatic, and hydrogen-bonding interactions. In contrast, the M-box RNA triggers a change in gene expression upon association with an undefined population of metals, rather than responding to only a single ligand. Prior biophysical experimentation suggested that divalent ions associate with the M-box RNA to promote a compacted tertiary conformation, resulting in sequestration of a short sequence tract otherwise required for downstream gene expression. Electrostatic shielding from loosely associated metals is undoubtedly an important influence during this metal-mediated compaction pathway. However, it is also likely that a subset of divalent ions specifically occupies cation binding sites and promotes proper positioning of functional groups for tertiary structure stabilization. To better elucidate the role of these metal binding sites, we resolved a manganese-chelated M-box RNA complex to 1.86 Å by X-ray crystallography. These data support the presence of at least eight well-ordered cation binding pockets, including several sites that had been predicted by biochemical studies but were not observed in prior structural analysis. Overall, these data support the presence of three metal-binding cores within the M-box RNA that facilitate a network of long-range interactions within the metal-bound, compacted conformation.

Introduction

All organisms require metal ions for many essential molecular functions, including catalytic mechanisms and cellular structural properties. It is injurious to bacterial growth when metal concentrations are inappropriately increased or decreased; therefore, specific mechanisms are required for maintaining intracellular pools. Metal-sensing regulatory (metalloregulatory) proteins coordinate metals with gene expression of transporters, metal-sequestering proteins, detoxification genes, and other factors.[1–3] Many examples of such metalloregulatory proteins have been discovered and characterized, mostly for control of transition metals. Less studied are regulatory mechanisms for the most prevalent ions in the intracellular environment of a bacterium, namely, potassium and magnesium, which are present at concentrations of approximately 110 mM and 0.5–1.0 mM, respectively.[4–7] More recently, two different

*Corresponding authors. E-mail addresses:
arati.ramesh@utsouthwestern.edu;
wade.winkler@utsouthwestern.edu.

Abbreviations used: NMIA, *N*-methylisatoic anhydride; AUC, analytical ultracentrifugation; SHAPE, selective 2′-hydroxyl acylation analyzed by primer extension; PDB, Protein Data Bank.

metal-sensing regulatory RNAs have been discovered to function as metalloregulatory elements for the control of magnesium homeostasis.[8,9] In both of these instances, increased magnesium levels resulted in an altered RNA structural conformation for an RNA element located within the mRNA 5′ leader region. This conformational change is coupled with the regulation of downstream genes. Understanding the molecular basis for these RNA-based mechanisms will provide important insights into metal-induced RNA folding pathways and will reveal the general importance of magnesium homeostasis control strategies.

Metal ions share a complicated relationship with nucleic acids,[10–13] playing a critical role in the formation of both secondary and tertiary structures. In general, positively charged metal ions aid in neutralization of the highly negative RNA backbone, enabling the formation of complex bends, folds, and long-range contacts characteristic of complex RNA structures. However, RNA-chelated ions have only been observed in small numbers; there are not enough ions to adequately shield the electronegative backbone by themselves. Instead, a concentration gradient of fully hydrated metals becomes aligned with the electrostatic potential surrounding the RNA, thus creating a diffuse "atmosphere" of ions. Various degrees of interaction between metal ions and RNA have been reported, ranging from loose or indirect association to direct coordination of the metal ion. The latter often involves the displacement of one or more water molecules from the inner-hydration shell of the metal ion and the substitution, instead, with functional groups from the RNA. Magnesium ions typically contact RNA oxygen atoms (mostly the nonbridging phosphoryl oxygens of the backbone) and, to a lesser extent, the 2′-OH groups of the ribose sugar and nucleobase oxygens (e.g., guanine O6 carbonyls and pyrimidine O4 groups). Less frequently, magnesium ions contact RNA nitrogens, such as the guanine N7 nitrogen.[14] It is through the cumulative effect of these interactions that many RNAs compact into their native conformational state. These interactions have been well illustrated by classic structural studies of ribozymes such as the P4–P6 domain of the group I intron and, more recently, riboswitch RNAs.

Riboswitches are cis-acting regulatory RNAs in bacteria that associate with metabolites and regulate expression of downstream genes.[15–18] They are generally composed of two portions: a signal-responsive aptamer domain and a downstream region that directly exerts regulatory control over proximal genes. Most often, the binding of the appropriate metabolite ligand is coupled with regulatory control of translation initiation or premature transcription termination,[15–19] although at least one riboswitch class controls the intracellular lifetime of its associated mRNA.[20] There are over 20 reported riboswitch classes that associate to a variety of small-molecule ligands, including amino acids, amino sugars, nucleobase-containing metabolites, and enzyme cofactors. Additionally, two different riboswitch classes have been discovered, which respond not to metabolites but to magnesium ions instead.[8,9] Specifically, the *Salmonella enterica mgtA* magnesium transport gene is subjected to regulatory control by a magnesium-responsive cis-acting RNA element located within the *mgtA* 5′ leader region. Also, the M-box RNA, which was originally described as an "orphan" riboswitch,[21] controls gene expression specifically in response to fluctuations of intracellular magnesium.[9] This function is consistent with the observation that the M-box riboswitch is typically located upstream of the three primary classes of magnesium transport genes: CorA, MgtA, and MgtE.[22] *In vitro* studies of the M-box riboswitch demonstrated that magnesium is capable of eliciting a dramatic conformational change for the aptamer domain.[9] However, this observation by itself is not surprising. Indeed, recent biophysical data have suggested that divalent ions alone can promote a near-native, compacted conformation for several riboswitch RNA classes, a structural configuration that resembles in part the final metabolite-bound state.[23–25] Although most riboswitches are likely to exhibit a structure-dependent relationship with monovalent and divalent ions, metal-dependent folding of the M-box RNA, by definition, must exhibit unique performance characteristics that enable it to function as a magnesium-responsive genetic element within the intracellular environment. Understanding the basis for regulation by the M-box riboswitch will help reveal the underlying principles used by metal-sensing regulatory RNAs in bacteria and may lead to the molecular engineering of synthetic metalloregulatory RNAs as genetically encoded metal sensors. Given the pivotal relationship between magnesium homeostasis mechanisms and bacterial pathogenesis,[7,26,27] the analysis of the M-box riboswitch is also likely to provide clues into the mechanisms used by intracellular bacterial pathogens for modulation of the divalent ion conditions within the phagosome where they reside.

Equilibrium measurements of folding of the M-box aptamer tertiary structure by hydroxyl radical footprinting and analytical ultracentrifugation (AUC) revealed that divalent ions triggered a compacted tertiary conformation.[9] Mutation of highly conserved residues prevented formation of this conformation. Also, the presence of cobalt(III) hexammine, which is isosteric with hexahydrated magnesium but is unable to make inner-sphere coordinations due to tight coordination of the amine ligands, did not elicit formation of the tertiary conformation. Together, these results suggested that individual cation sites were specifically required for tertiary structure formation, including a requirement

for inner-sphere coordinations to RNA. From these data, it is unlikely that loosely associated, nonspecific cation interactions alone are responsible for the compacted native conformation. Therefore, elucidating and characterizing specific cation binding sites is crucial for understanding the molecular mechanism of the M-box riboswitch.

One of the most successful methods in identifying specific RNA–metal interactions at high resolution is X-ray crystallography of metal-bound RNA complexes. For example, an analysis of metal ions associated with the large ribosomal subunit revealed the presence of 116 magnesium and 88 monovalent ions, most of which included at least one inner-sphere coordination to RNA atoms.[28] At many of these sites, metal–RNA interactions appeared to position the nucleoside and phosphoryl groups in optimum orientations for facilitation of noncanonical interactions and long-range tertiary contacts. Similarly, a total of six well-ordered magnesiums were observed in a 2.7-Å structural model of a representative M-box RNA determined by X-ray crystallography.[9] Most of these ions also appeared to position nucleosides for tertiary contacts, suggesting that they might be important for the compact, tertiary conformation. However, the relative importance of each metal site is unclear from this structural model alone. It is also possible that the folding pathway of the M-box RNA may involve specific cation sites in addition to those observed from the structural model. Indeed, metal–RNA interactions are undoubtedly more dynamic than can be implied from a single structure, making it difficult to establish the functional relevance of individual cation binding sites from structural data alone. A commonly used biochemical method for assessing the importance of individual metal ion binding sites is through substitution of phosphoryl oxygen atoms with sulfurs,[29,30] which exhibit a marked decrease in affinity for magnesium ions.[31] If the sulfur substitution coincides with a loss of function of the RNA molecule, it is generally presumed that the substitution ablated an important magnesium site. However, alternative explanations for such phosphorothioate substitutions are still possible, including perturbation of local structural features by the sulfur atom. Previously, we searched for randomly substituted phosphorothioates that prevented magnesium-mediated compaction of the M-box RNA,[32] and we observed remarkable agreement between the sites of phosphorothioate interferences and the six magnesium sites observed in the prior structural model. However, we also observed a small collection of phosphorothioate interferences within electronegative pockets that resembled cation sites, but which lacked metals in the structural model. Based on this observation, we proposed a role for these sites as putative metal sites, perhaps operative during folding of the M-box RNA. An additional method for investigating magnesium sites is through substitution with manganese. Typically, manganese can substitute for magnesium; however, the ability of manganese to bind to a particular RNA site may not necessarily prove it to be a magnesium site as the two ions exhibit different chemical characteristics.[33–36] In this study, we investigated Mn^{2+}-chelated M-box complexes by X-ray crystallography, using Mn^{2+} to substitute Mg^{2+} in the M-box structure. The anomalous scattering properties of Mn^{2+} have been used to independently locate Mn^{2+} sites in the M-box structure. Our data suggest that the M-box RNA binds Mn^{2+} with a higher affinity as compared to Mg^{2+}, suggesting that certain divalent binding sites, which were not visualized in the Mg^{2+}-bound structure of the M-box, might be visualized with Mn^{2+} in the crystal structure. Here, we confirm the presence of at least eight functionally relevant Mn^{2+} ions bound to the M-box, six of which were previously observed in the Mg^{2+}-bound complex and others that agree well with phosphorothioate interference patterns. These data also reveal a higher-resolution structural model, at 1.9 Å, and include a second, modestly altered conformation that appears to result from the lack of metal occupancy at several magnesium sites, thereby emphasizing their functional significance. From the sum of all of these data, we gain a more thorough understanding of the specific magnesium sites that are formed within the M-box tertiary structure, which are likely to play a critical role during metal-responsive regulation by M-box RNAs.

Results

Mn^{2+}-induced folding of the *Bacillus subtilis* M-box aptamer

Divalent metal ions associate closely with RNA, occupying specific sites and serving to neutralize negatively charged pockets in the RNA. This charge neutralization likely stabilizes tertiary contacts and folding of the RNA. The global effect of Mg^{2+} on the conformation of the *B. subtilis* M-box aptamer has been characterized previously[9] (Fig. 1a and b). However, in this study, we wanted to compare the folding characteristics of M-box in the presence of different ions and to elaborate on the interactions of other divalent ions with the M-box using structural probing techniques. First, the compaction of the M-box RNA in response to increasing concentrations of Mg^{2+}, Mn^{2+}, and Ca^{2+} was quantified using AUC (Fig. 1c). In the presence of 100 mM monovalent ions, the compacted form of the RNA was induced by Mn^{2+} with a half-maximum change (EC_{50}) occurring at 0.1 mM. This compares to a value of 0.4 mM for Mg^{2+} and Ca^{2+}, suggesting a fourfold higher overall affinity for binding Mn^{2+} as

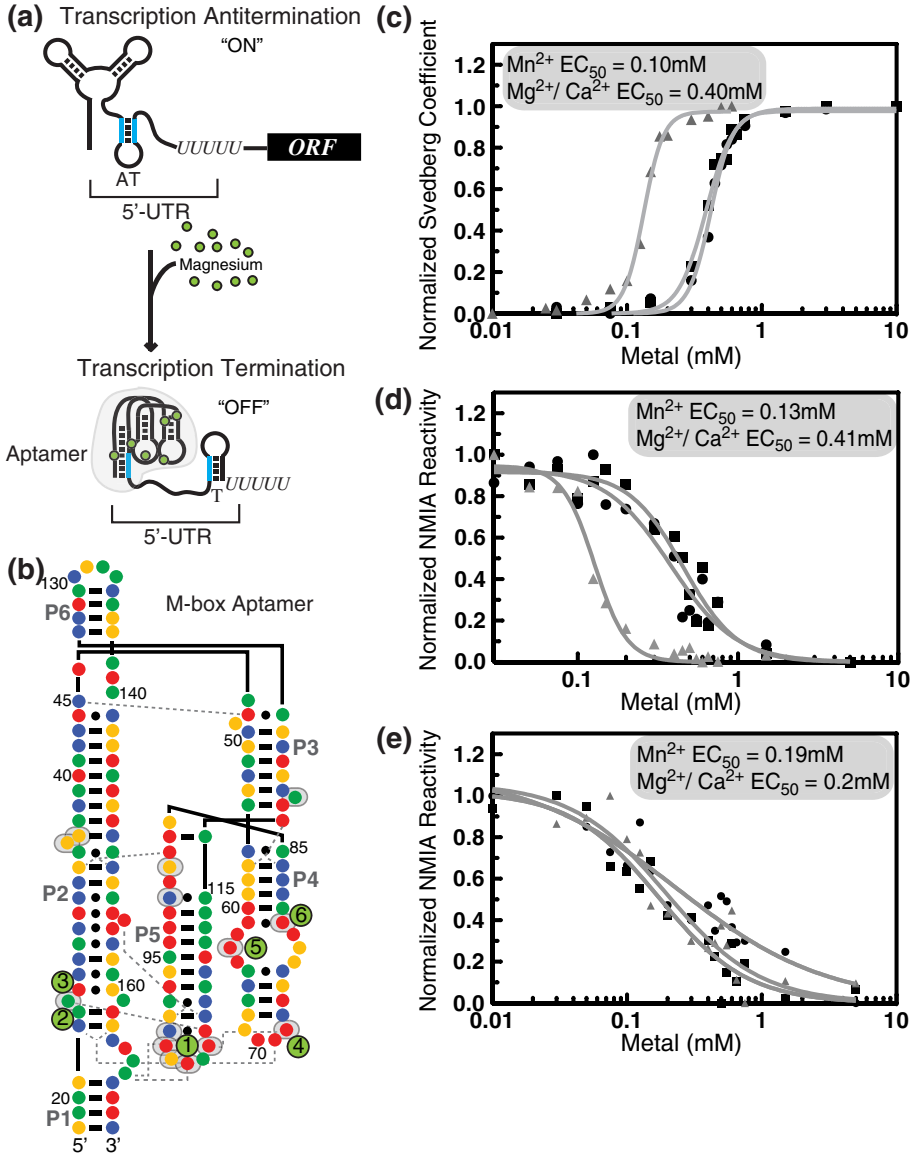

Fig. 1. Metal-dependent compaction of the M-box RNA. (a) Schematic representation of the mechanism for Mg^{2+} sensing by the M-box riboswitch. Under conditions of low Mg^{2+}, an antiterminator (AT) helix is formed (shown as blue lines) within the mRNA leader region. Under conditions of high Mg^{2+}, the aptamer folds into a conformation that sequesters the left half of the AT and permits the formation of a downstream termination site (T). (b) Sequence and secondary structure of the *B. subtilis mgtE* M-box aptamer RNA used in this study. Circles that are yellow, green, red, and blue correspond to C, U, A, and G, respectively. Broken lines indicate key tertiary contacts. Numbered green circles denote six Mg^{2+} observed in the previously published structural model.[9] Circled residues correspond to the sites of phosphorothioate interferences[32] _ENREF_31. (c) AUC of M-box aptamer RNA shows compaction of the RNA, represented by a change in the Svedberg coefficient induced by Mg^{2+} (circles), Mn^{2+} (triangles), and Ca^{2+} (squares) in the presence of 100 mM potassium chloride. Compaction of the M-box is achieved at lower concentrations (EC_{50} = 0.1 mM) of Mn^{2+} as compared to Mg^{2+} and Ca^{2+} (EC_{50} = 0.4 mM). (d and e) SHAPE probing[37] _ENREF_32 of the M-box aptamer upon incubation with increasing divalent metals, shown as a plot of normalized NMIA reactivity *versus* metal ion concentration. Reactions are shown for (d) physiological (100 mM) and (e) high (2.1 M) concentrations of monovalent ions. Positions that decrease in reactivity with NMIA in the presence of Mg^{2+} (circles), Mn^{2+} (triangles), and Ca^{2+} (squares) are shown. Curve-fitting analysis indicates an EC_{50} value of 0.41 mM for $Mg^{2+}$and Ca^{2+} and an EC_{50} value of 0.12 mM for Mn^{2+} in the presence of low monovalents. This difference is eliminated in the presence of high concentrations of monovalent ions.

compared to Mg^{2+} and Ca^{2+}. The Hill coefficients for these fits, however, showed similar values (ranging from 4.3 to 5.5) regardless of the metal bound. This suggests that the M-box may bind different metal ions with similar degrees of cooperativity but with varying affinity.

To further characterize metal-induced structural changes in the M-box, we employed selective 2′-hydroxyl acylation analyzed by primer extension (SHAPE)[37] (Fig. 1d and e). In this technique, *N*-methylisatoic anhydride (NMIA) forms a covalent adduct with 2′-hydroxyl groups in a structure-dependent manner. We measured the NMIA reactivity of M-box riboses in response to increasing concentrations of Mg^{2+}, Mn^{2+}, or Ca^{2+} and in the presence of physiological (100 mM) or high (2.1 M) monovalent ions. These data show that, in the presence of molar concentration of monovalents, all three divalents induce compaction of the M-box RNA at nearly identical concentrations. However, in the presence of 100 mM monovalents, the M-box RNA was compacted at a lower concentration of Mn^{2+} (EC_{50} of 0.13 mM) as compared to Mg^{2+} and Ca^{2+} (EC_{50} of 0.4 mM). Together, these results suggest that the M-box compacted state can be induced by multiple divalent ions, albeit at different concentrations. In the cellular context, this difference in affinity may be overcome by the relative abundances of each metal ion, with the M-box functioning as a Mg^{2+}-responsive genetic switch due to the elevated levels of Mg^{2+} relative to other metal ions. However, metal-induced folding of the M-box RNA was similar for the different divalents in the context of high monovalent ions, suggesting that a common minimal number of divalent cation sites were required when low-affinity metal interactions could be outcompeted by monovalent ions.

Global arrangement of the Mn^{2+}-chelated M-box aptamer

Having confirmed that the overall fold of the M-box is similar in the presence of Mn^{2+} and Mg^{2+}, we identified conditions for crystallographic analysis of the M-box aptamer in the presence of 5 mM Mn^{2+} instead of Mg^{2+}. While this substitution resulted in the formation of crystals, the addition of 50 mM ammonium sulfate as an additive significantly improved diffraction quality. The previously reported 2.7-Å structural model revealed that the M-box forms a three-helical arrangement in the Mg^{2+}-bound conformation.[9] This compacted native state appeared to be stabilized by multiple long-range nucleoside and base-stacking interactions. Six well-ordered Mg^{2+} ions were identified in the structural model, which appeared to assist many of the long-range interactions. Four of these cation sites (Mg1–Mg4) are located within a common region at the base of the molecule where the three helical elements converge. The remaining two cation sites were located within an internal bulge of the P4 helix. A selection for phosphorothioate substitutions that prevented Mg^{2+}-mediated compaction revealed that each of these six cation sites is functionally required for the compact conformation.[32] Also, the general strength of phosphorothioate interferences moderately agreed within these two cation binding "cores", with core 1 consisting of four cation pockets (M1–M4) and core 2 consisting of the region encompassing two such sites (M5–M6). Core 1 appears to stabilize key inter-helical interactions at the portion where the three helices converged. Core 2 may assist orientation of the L4 terminal loop to permit key long-range interactions. However, additional phosphorothioate interferences were identified at positions other than within the binding sites for M1–M6. Several of these sites, which exhibited a similar overall strength of phosphorothioate interference, were found to be located within electronegative cavities reminiscent of the other cation binding pockets. From these data, we proposed the presence of three additional metal binding sites (M7–M9). These putative metal sites were found to cluster at the apex of the molecule ("core 3") and appeared to be poised to stabilize important inter-helical interactions. However, the sites in core 3 were unoccupied in the Mg^{2+}-bound M-box structural model. It is possible that these electronegative cavities represent relatively low-occupancy sites and therefore were not observed in the 2.7-Å structure. To further investigate these additional putative metal sites, we solved the crystal structure of the M-box RNA in the presence of Mn^{2+}, thereby exploiting two features of Mn^{2+}: its ability to occupy Mg^{2+} sites in RNA structures and its behavior as an anomalous scatterer of X-rays. This latter feature permitted the unequivocal identification of divalent ion binding sites.

Crystals of the M-box RNA grown in the presence of 5 mM Mn^{2+} diffracted to 1.9 Å, thus providing higher-resolution data than the previous Mg^{2+}-bound structure. A representative electron density for these data is shown in Fig. 2c. The asymmetric unit was composed of two molecules (hereon referred to as chain A and chain X) that exhibited subtle structural differences. These two molecular conformations also exhibited differences in the total number of Mn^{2+} sites that were occupied. The overall structure of the Mn^{2+}-bound M-box RNA resembled closely that of the Mg^{2+}-chelated complex. The overlay of chain A of the Mn^{2+}-bound structure with the Mg^{2+}-bound structure (Fig. 2a) suggests an RMSD of 0.9 $Å^2$ for the superimposed backbone atoms. Interestingly, superimposition of chain A and chain X of the Mn^{2+}-bound M-box (Fig. 2b, RMSD = 0.7 $Å^2$) shows structural differences in the L4 loop, from position A61 to position C68. This region of the M-box is involved in multiple long-range contacts that are centered on M5 and M6 in core 2. The apparent flexibility of the M-box backbone in this region may support the previous observation that metal sites in core 2 show relatively weaker phosphorothioate interference.[32] Consistent with this, chains A and X show not only altered backbone conformation in this region but also different Mn^{2+} occupancies; the M5 and M6 metal

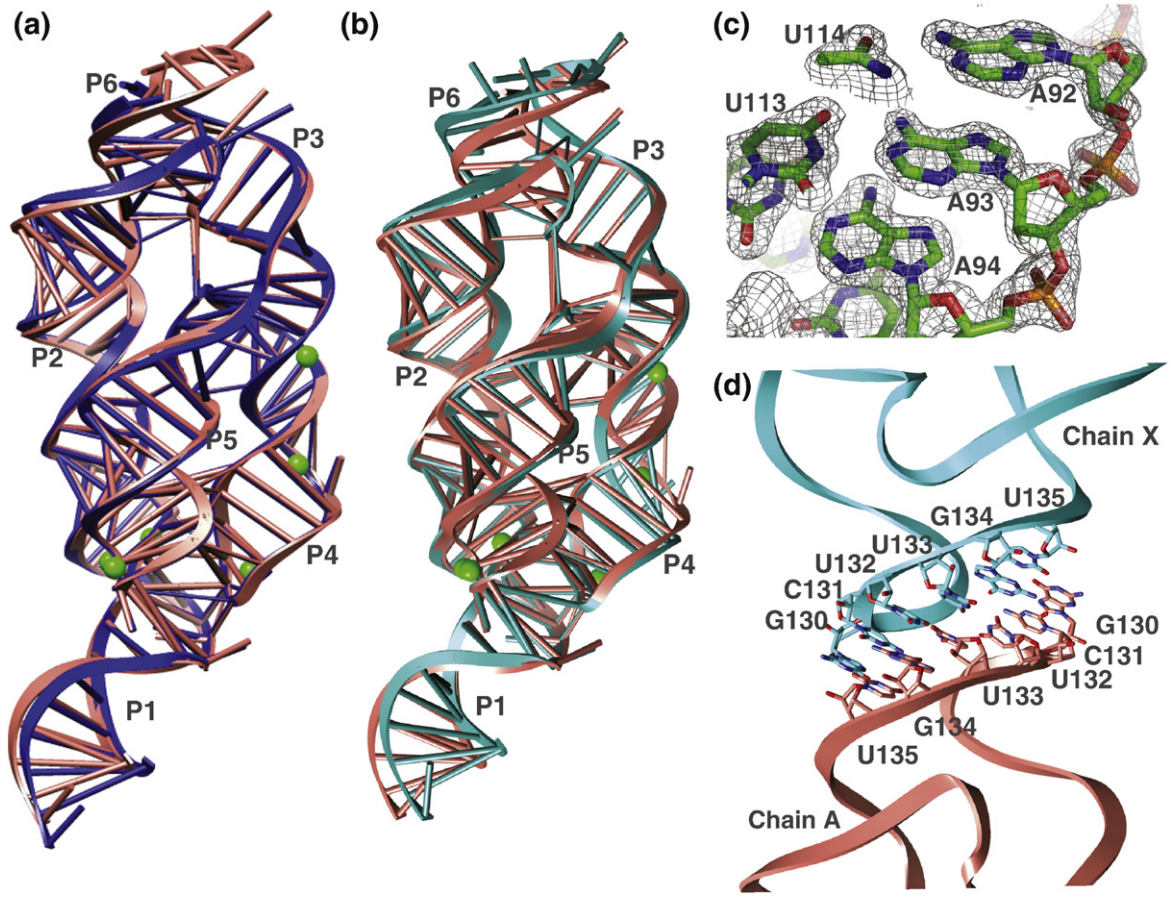

Fig. 2. Overall structure of the Mn^{2+}-bound M-box. (a) Chain A of the two molecules in the asymmetric unit of the Mn^{2+}-bound M-box structure (pink) superimposed with the Mg^{2+}-bound M-box (blue) shows negligible differences in the backbone and side-chain conformations. Mg^{2+} ions observed in the Mg^{2+}-bound structure are shown in green. (b) The two molecules in the asymmetric unit of the Mn^{2+}-bound M-box are superimposed with chain A (pink) and chain X (cyan). (c) Representative portion of the Mn^{2+}-bound M-box structural model is shown (stick representation) with $2F_o - F_c$ map (mesh) contoured at 1.5 σ. (d) Details of interactions observed in the P6 helix are shown. Symmetry-related molecules form intermolecular kissing loops interaction to stabilize the P6 helix in this crystal form.

sites in core 2 are only occupied for chain A, which shares identical structural arrangement with the Mg^{2+}-bound structure.

The P6 helix region of the molecule was disordered in the previous structural model. However, increased resolution and different space group symmetry in the Mn^{2+} crystals allowed visualization of the P6 helix. Intermolecular kissing loop interactions between symmetry-related molecules appeared to stabilize the L6 loop (Fig. 2d). The loop–loop interaction involves six nucleotides (G130, C131, U132, U133, G134, and U135), where G–U and G:C base pairs flank the central uridines and allow them to be stabilized by N3–O4 and O2–N3 interactions, respectively. While it is likely that the relative orientation of these nucleotides with respect to the native M-box structure may be affected by this crystal contact, the increased order in this region resulted in an improved electron density of the entire P6 helix region. The increased resolution extended beyond the six nucleotides involved in the kissing loop, thereby permitting visualization of the P6 helix, which was previously not modeled for the Mg^{2+}-bound M-box structure from lack of clear electron density.

X-ray diffraction data collected at the absorption edge of Mn^{2+} allowed the calculation of anomalous difference Fourier maps. This allowed for the direct placement of Mn^{2+} ions in the M-box crystal (Fig. 3a). Guided by difference density calculated from 1.9-Å-resolution data, we modeled key water molecules that coordinate Mn^{2+} into the Mn^{2+}-bound M-box structure. The geometry of these sites provided further confirmation for the presence of fully coordinated Mn^{2+} ions in the M-box RNA structure. The different Mn^{2+} sites in the two chains exhibited a range of strengths for positive anomalous difference density. The two chains also differed

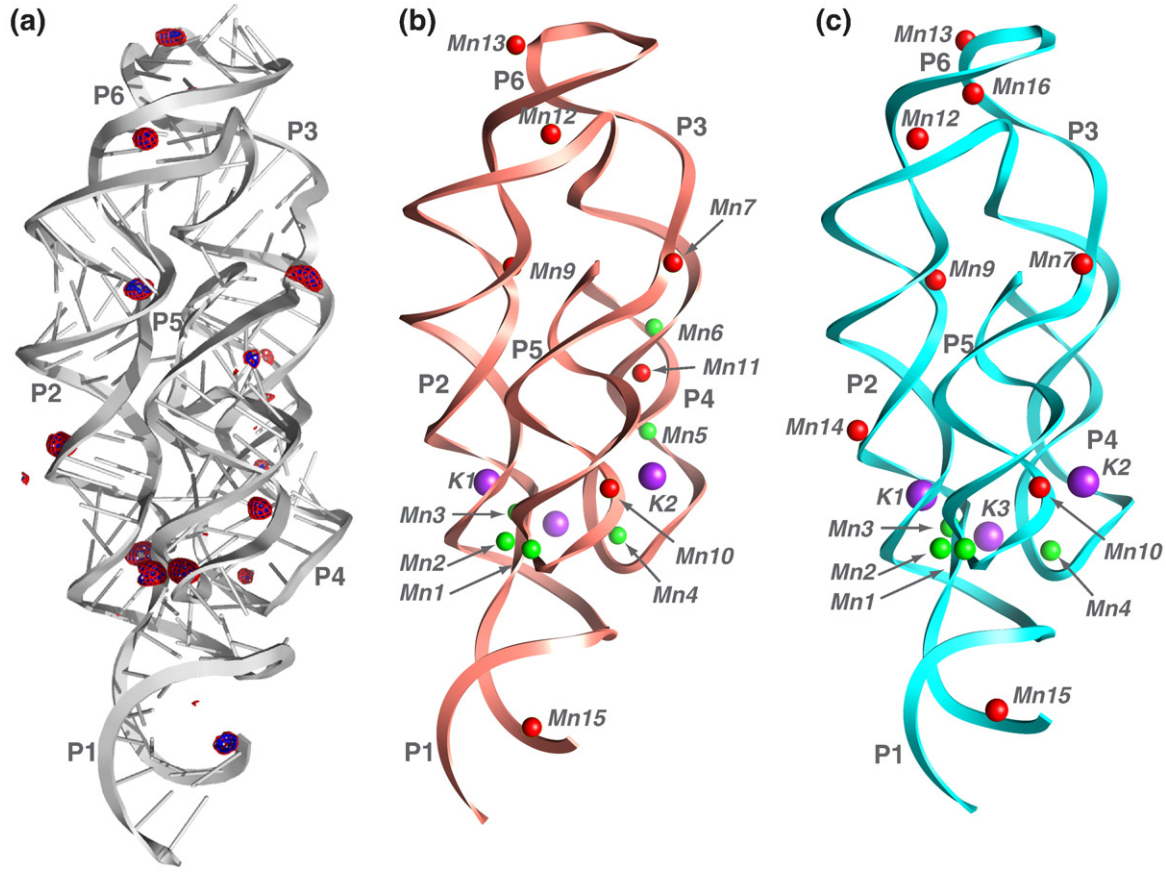

Fig. 3. Locating Mn^{2+} ions in the M-box structure. (a) The Mn^{2+}-bound M-box structure is shown (gray) with the anomalous difference Fourier (mesh) contoured at 7 σ (red) and at 4 σ (blue). (b) Chain A in the Mn^{2+}-bound M-box is shown with potassium ions (purple), previously identified divalent sites (green), and newly identified divalent sites (red). (c) Chain X of the Mn^{2+}-bound M-box is shown with the metals observed in the structural model.

modestly in the number of occupied metal sites (Fig. 3b and c).

Mn^{2+} occupies Mg^{2+} sites in the core 1 and core 2 regions

We compared the core 1 from the previously solved M-box structure to each of the two chains in the Mn^{2+}-bound M-box. Three out of four sites in core 1 (M1, M2, and M3) showed nearly identical occupancies in both chains. Mn1 was coordinated via interactions to the RNA backbone with the nonbridging phosphate oxygens of G100, C102, and A103, at an average distance of 2.18 Å. Similar to the Mg^{2+}-bound structure, another key coordination occurred through the nucleobase oxygen of U104. Two water molecules completed the hexa-coordinate state of Mn^{2+}, at distances of 2.3 Å. Coordination of Mn2 occurred via two inner-sphere interactions with backbone phosphate oxygens of U23 and G100 and was confirmed with Mn^{2+} anomalous density of 13 σ. Again, distances from the remaining coordinating water molecules averaged around 2.25 Å, slightly higher than the 2.15 Å seen for the Mg^{2+}-bound structure. Mn2 is also coordinated via an outer-sphere interaction with a backbone phosphate oxygen of G157, similar to what was observed for the Mg^{2+}-occupied site. This interaction is likely to be functionally significant as previous phosphorothioate interference experiments had inferred the importance of this outer-sphere interaction.[32] Mn^{2+} occupancy at the M3 cation site, which was coordinated via two inner-sphere interactions with U24 and A25 phosphate oxygens, was confirmed by the presence of Mn^{2+} anomalous density of 16 σ. In total, these data agreed well with previous experiments, wherein nucleotides involved in coordinating Mg^{2+} at these three sites exhibited strong phosphorothioate interferences of nearly identical intensities.[32] Moreover, Mn^{2+} sites 1, 2, and 3 were superimposable with the corresponding Mg^{2+} sites (Fig. 4b), with negligible change in position of not only the metal ion but also the coordinating water molecules. This suggests that certain M-box Mg^{2+} sites can be substituted with Mn^{2+} without

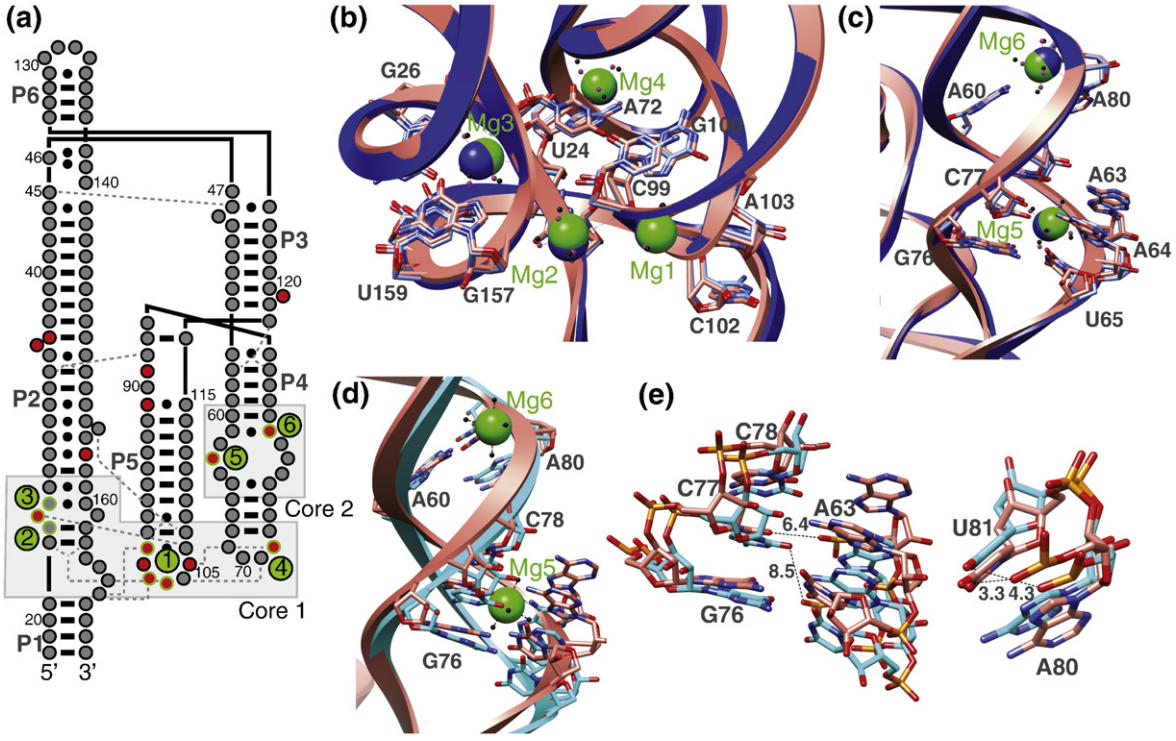

Fig. 4. Mn^{2+} ions occupy previously established Mg^{2+} sites from core 1 and core 2 of the M-box. (a) Secondary structure of the *B. subtilis mgtE* M-box. Red positions denote sites of phosphorothioate interferences. Broken lines denote key tertiary interactions. Green coloration denotes previously established Mg^{2+} sites and their inner-sphere interactions. (b) The Mn^{2+}-bound M-box (pink) superimposed with the Mg^{2+}-bound M-box (blue) for the region surrounding the metal sites in core 1. There are negligible structural differences in the backbone and individual nucleotide orientations. Mn^{2+} ions (green) and metal-coordinating water molecules (black) in the Mn^{2+}-bound M-box are shown along with Mg^{2+} ions (blue spheres) and metal-coordinating water molecules (magenta) from the Mg^{2+}-bound M-box structures. (c and d) Metal sites M5 and M6 in core 2 are shown in a color scheme similar to (a) with Mn^{2+}-bound chain A (pink) or chain X (cyan) superimposed on the Mg^{2+}-bound M-box (blue). (e) The details of interaction around metal site 5 (left) and metal site 6 (right) are shown, with distances marked in Angstroms.

distortion of the site geometry and positions of the coordinating ligands from the RNA. Finally, the last remaining core 1 cation site (Mn4) was coordinated by a single inner-sphere contact to a nonbridging phosphate oxygen of A72 and by an outer-sphere contact to the N7 of A72. It is noteworthy that this site is likely to represent the weakest specific cation site in core 1, since the anomalous density ranged from 3.8 σ in one chain to 5.8 σ in the other chain. Consistent with this, position A72 had previously exhibited only moderate phosphorothioate interference.

In contrast to core 1, we observed moderate structural differences between chain A and chain X in the Mn^{2+}-bound M-box within the core 2 region (Fig. 4c). Whereas chain A permitted substitution of Mg^{2+} sites with Mn^{2+}, chain X showed a different backbone conformation in the vicinity of sites M5 and M6, which were unoccupied by Mn^{2+} in the latter molecule. In general, the chain A M5 and M6 sites also showed weaker Mn^{2+} anomalous peaks (~5.5 σ) relative to M1–M3. Superposition of Mn5 and Mn6 in chain A with those in the Mg^{2+}-bound M-box (Fig. 4b) revealed a high degree of structural conservation. Mn5 contacts the RNA though one inner-sphere interaction with the phosphate oxygen of A63 and multiple outer-sphere interactions with nucleobases of C77 and U75. However, while the distance between these atoms is ~6.4 Å (O2P of A63 to O2 of C77) in chain A, it is ~8.5 Å in chain X (Fig. 4d), thereby positioning the metal-chelating ligands too far from one another for the formation of the cation pocket. Similarly, Mn6 is coordinated by a backbone phosphate oxygen of A80 and the O4 of U81. The two metal-coordinating atoms are 3.3 Å apart, allowing the formation of a relatively more compact cation binding pocket. In chain X, however, this distance is 4.4 Å, thereby eliminating this cation site.

Mn^{2+} occupies a subset of the putative sites within core 3

Previously, we had observed phosphorothioate interferences at positions C35, C36, C89, G91, and U119 in the M-box aptamer.[32] These positions

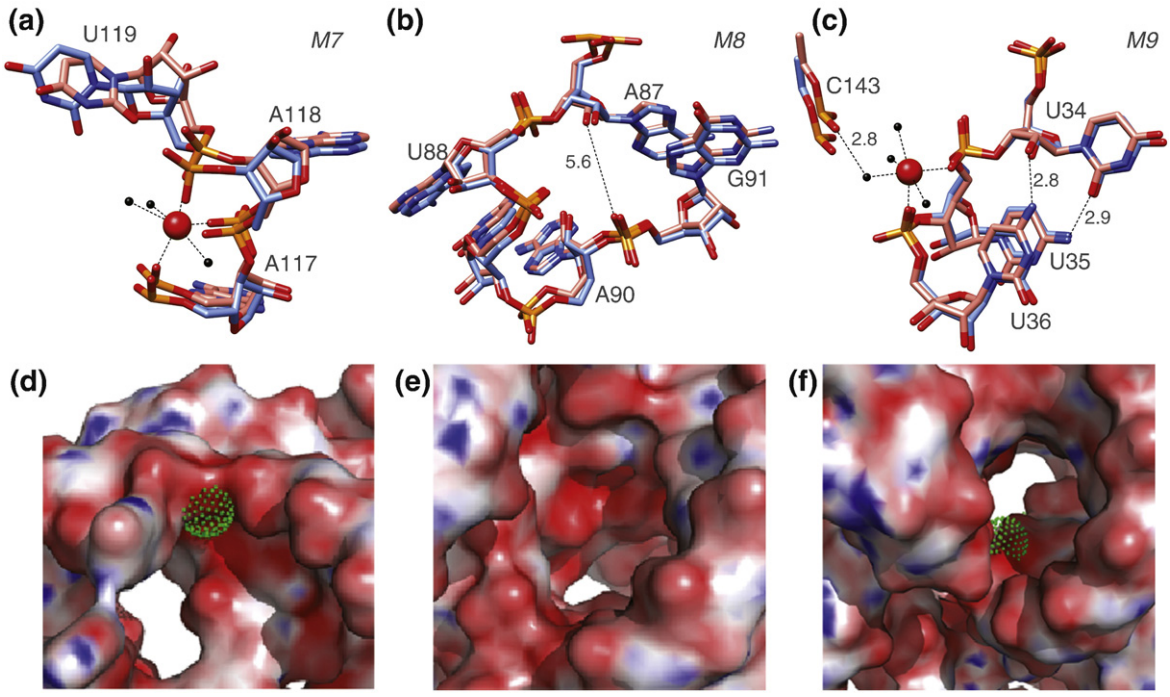

Fig. 5. Mn^{2+} occupies sites M7 and M9 but not site M8 in core 3. (a–c) The details around metal site Mn7, putative site M8, and metal site Mn9 are shown with Mn^{2+} ions as red spheres. Broken lines mark distances in Angstroms. Key coordinating functional groups are shown along with metal-coordinating water molecules (black). (d–f) Surface representation of the corresponding metal sites 7, 8, and 9 in the Mn^{2+}-bound M-box are shown and colored by electrostatic potential. Cation binding sites are visible as patches of relatively higher electronegativity.

showed similar degrees of interference and, when mapped on to the structure of M-box, were found to cluster around the apex of the three-helical bundle that forms the architectural foundation of the molecule. These positions together appeared to represent three putative metal sites, which we designated M7 through M9. However, in the crystallographic model of the Mg^{2+}-chelated M-box aptamer, the sites were not occupied by metal. One possible explanation is that they exhibit relatively low affinity for metal ligand and, therefore, were unoccupied in the final crystal structure. Alternatively, the putative M7–M9 sites might be occupied with metals only during folding. Since the overall affinity of M-box for Mn^{2+} was higher than that for Mg^{2+}, we considered the possibility that Mn^{2+} might exhibit higher affinity at specific cation binding sites in the M-box. Therefore, we examined the Mn^{2+}-bound M-box structure for Mn^{2+} anomalous density in the predicted metal sites M7–M9. The M7 and M9 sites exhibited clear anomalous density of 7 σ and 11 σ, respectively (Fig. 3a), while M8 exhibited very weak anomalous density, and a metal could not be modeled with enough confidence (Fig. 5b).

A closer examination of Mn7 (Fig. 5a) showed that it is coordinated by three backbone interactions with phosphate oxygens of A117, A118, and U119. Of these, the interaction with U119 alone was via the pro-Rp oxygen and was previously seen as a position of phosphorothioate interference. Metal–ligand distances are in the range 2.3 Å, as seen for the other Mn^{2+} sites. Three water molecules, at an average distance of 2.5 Å, complete the Mn^{2+} coordination. The combined orientations of the A117, A118, and U119 phosphates toward formation of an electronegative cavity appeared to help position adjacent nucleosides for key long-range interactions at the apex of the molecule. For example, the nucleobase ring of A118 stacks against the G56–U85 base pair located in the backbone U-turn separating the P4 and P5 helices. Long-range interactions in this region of the M-box are likely to be critical for stabilization of the sharp, 180° turn required between the P4 and P5 helices. Similarly, A117 stacks against the A87–U116 base pair at the apex of the P5 helix and also forms an A-minor motif interaction with the P4 G84–C57 base pair, again stabilizing distant regions of the RNA.

Mn9 is coordinated by inner-sphere interactions with the pro-Rp oxygens of C35 and C36 (Fig. 5c). Outer-sphere interactions with the phosphate oxygens of C143 from the adjacent turn of the P2 helix further stabilize this coordination. Considering the placement of this Mn^{2+} site, it is possible that it influences the turn of the P6 helix, allowing the M-box to fold upon itself and to form the three-helical

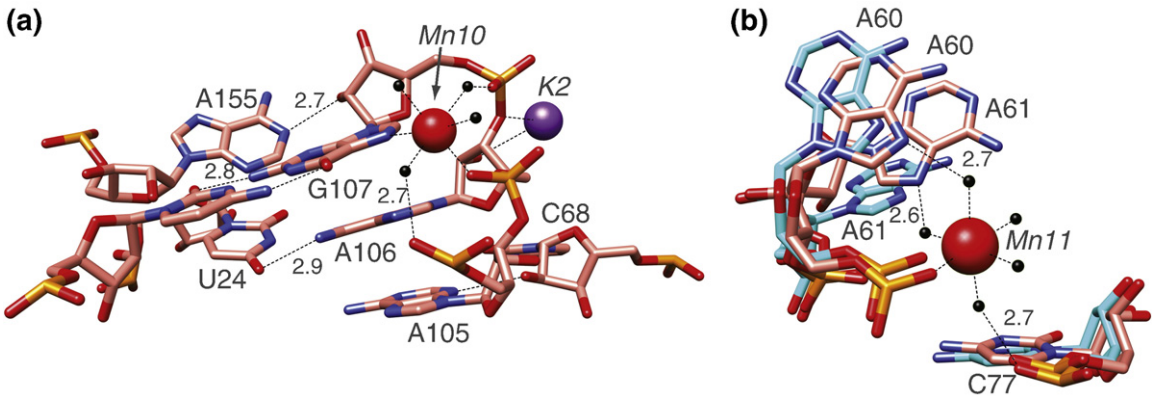

Fig. 6. New metal sites that may be functionally relevant. (a) The divalent metal site around Mn10 of chain A of the Mn^{2+}-bound M-box structure is shown with Mn^{2+} ions (red), potassium ions (purple), and water molecules (black). Broken lines mark distances in Angstroms. (b) Superposition of metal site Mn11 is shown with chain A (pink) and chain X (cyan) of the Mn^{2+}-bound M-box. The site in chain X (cyan) was not occupied by Mn^{2+}, most likely due to differences in backbone conformation as shown herein.

bundle. C35 not only makes direct inner-sphere contacts with Mn9 but also stacks against A88, which is involved in an A-minor interaction to a P2 G:C base pair. These different metal sites exhibit a concentration of electronegative charge as would be expected for specific cation binding sites (Fig. 5d–f).

New metal sites

Having visualized Mn^{2+} anomalous density in the six Mg^{2+} sites observed previously in the Mg^{2+}-bound M-box structure and having confirmed two of the three putative metal sites predicted by phosphorothioate substitution experiments, we next examined the structure for additional anomalous density. Several new sites of Mn^{2+} occupancy were observed (Fig. 3b). In total, we observed six additional Mn^{2+} ions, labeled herein as Mn10–Mn15. Most were observed in both RNA chains, although Mn11 was present only in chain A, and Mn14 was present only in chain X.

The most interesting of these metal sites, Mn10, is present in the L5 loop and is coordinated via one backbone interaction with the pro-Rp oxygen of A106 and the N7 of G107 (Fig. 6a). Two outer-sphere interactions with pro-Rp oxygen of A105 and G107 further stabilize the coordination. Notably, A105 had previously shown to exhibit moderate phosphorothioate interference. Also, O2 of A106 on the nonmetal binding face coordinates a potassium ion. The ribose oxygen of G107 further interacts with N1 of A155 from the P2 helix. The adenine rings of A105 and A106 stack against each other and interact on opposite faces with elements from L4 and P2. While the A105 nucleobase interacts with the C68 ribose oxygen from the L4 loop, the N6 of A106 lies within 2.87 Å of the U24 O4, located in the P2 helix. The G107 ribose oxygen further interacts with N1 of A155, which is also located within the P2 helix. Given the importance of these tertiary interactions, it is possible that Mn10 may represent a functionally important metal ion that was previously not observed in the Mg^{2+}-bound form of the M-box.

Mn11 is present in the P4 helix of the M-box aptamer, making one inner-sphere contact with the A60 phosphate oxygen (Fig. 6b). The remaining coordinations are satisfied by water molecules. Outer-sphere coordinations are also seen with the N7 groups of A60 and A61 and the phosphate oxygen of A77. As seen with the other Mn^{2+} sites in the P4 helix (Mn5 and Mn6), Mn11 is present only in chain A and not in chain X. In chain X, the altered backbone conformation in the P4 helix alters the placement of the nucleotides involved in coordinating Mn11, placing them too far away to be able to create a compact metal-coordinating pocket. Mn11 also shares yet another feature with Mn5 and Mn6 in metal core 2; the strength of anomalous density at around 6 σ in all three sites is similar (Fig. 3a).

Mn12 lies at one end of the P2 helix, close to the L6 turn in the M-box aptamer. Both chains showed occupancy of Mn^{2+} ions in the site. However, the position of this Mn^{2+} ion differed between the two chains. Chain A resembled the Mg^{2+}-chelated M-box structure in this region with regard to the arrangement of backbone atoms. Here, the Mn^{2+} ion is coordinated by an inner-sphere interaction with a phosphate oxygen of G45 (distance of 2.2 Å), which makes important contacts with U140. The N7 of G45 also makes an outer-sphere contact with Mn12. The remaining coordinations are satisfied via water molecules, though only four of the five metal-chelating water molecules were modeled due to lack of clear density for one water molecule. A46 forms multiple interactions with A139 and U138 on the same plane, with a distance of 2.96 Å between the

N6 of A46 and the O2 of U138. U138 is positioned so as to make an outer-sphere contact to Mn12 via a water molecule. In chain X, however, the location of Mn12 is different. The Mn^{2+} is coordinated via inner-sphere interactions with the N7 of G45 (distance of 2.5 Å), whereas the phosphate oxygen on G45 makes an outer-sphere contact via a metal-chelating water molecule. This region of the RNA shows one more significant difference with regard to the structure of chain A. A46 is splayed outward from the P2 helix, and instead of interacting with A139 on the plane of the nucleobase, it stacks against the adenine ring. Also, the interaction between A46 and U138 is altered such that the N6 of A46 is positioned as far away as 5.23 Å from the O2 of U138.

Mn13 is present in the P6 helix, proximal to the L6 loop, and is coordinated to the pro-Sp phosphate oxygens of G127, A128, and U129 and two water molecules. Hexa-coordination is completed by water from the other chain. Also noteworthy is an outer-sphere interaction with G29 from the other chain via a water molecule. This observation suggests that this site is created due to the proximity of the two chains of the M-box in the crystal lattice and, therefore, not likely to be of functional relevance. Mn14 is present in the central region of the P2 helix, coordinated by nucleotides A30 and G31 that stack against each other in the P2 helix. The proximity of a symmetry-related molecule in this region, lack of apparent metal-mediated tertiary contacts, and lack of phosphorothioate interference data for the coordinating nucleotides seem to suggest that this site is not likely to be functionally relevant. Mn15 is coordinated via the N7 of G15 and is in close proximity to the pro-Sp oxygen of G15. Mn16 is occupied only in chain X and is coordinated via the N7 of G126 and the ribose oxygen of A46. Moderate anomalous density (~6 σ) prompted us to assign these sites as Mn^{2+} sites; however, there is lack of clear density for the assignment of metal-coordinating water molecules.

Discussion

Metal ions play a critical role in RNA tertiary structure formation and often mediate long-range interactions between distant regions of the RNA. Recent data suggest that many riboswitches are influenced by Mg^{2+}[23,25,38,39] and adopt a Mg^{2+}-dependent native or near-native state, even in the absence of their metabolite ligands. In this regard, the M-box RNA is unique, wherein it has evolved to couple global, Mg^{2+}-dependent compaction to signal-responsive gene regulation. It is therefore no surprise that, unlike other riboswitches that recognize a single ligand molecule, the M-box associates with several putative ligand molecules. It is likely that the M-box relies on more than just a diffuse atmosphere of loosely associated ions for overall charge neutralization (a function that can be performed by most positively charged ions regardless of valency) and structural compaction; our data suggest that the M-box native state is dependent on the formation of specific cation binding pockets. These cation binding sites are likely to be responsible for sensory input during regulation by M-box riboswitches. The challenge thus far has been to identify the dedicated cation binding sites within the M-box and to assess the importance, affinity, and specificity of each individual site with regard to the M-box function.

The previously determined crystallographic structure of a Mg^{2+}-bound M-box revealed the global architecture of the M-box and identified six key Mg^{2+} binding sites. Follow-up biochemical experiments confirmed the importance of these six sites and predicted three additional putative binding sites. These latter sites were unoccupied in the Mg^{2+}-bound crystal structure of M-box, suggesting that they likely represent low-occupancy sites or are transient sites that might play a role in the formation of higher-occupancy cation sites of core 1.

In the current study, we have attempted to visualize the complete suite of specific cation binding sites in the M-box. Based on phylogenetic analyses, the majority of M-box RNAs is predicted to mediate Mg^{2+} ion homeostasis.[22] However, visualization of Mg^{2+} ions in crystal structures poses inherent difficulties, since Mg^{2+} ions and water molecules share similar number of electrons and cannot be resolved easily in the electron density map. This is especially challenging with lower-resolution X-ray diffraction data. Most often, it is the geometric constraints of a Mg^{2+} ion in a cation binding site that help identify Mg^{2+} ions in a crystal structure. To unambiguously assign the cations bound to M-box, we solved the structure in the presence of Mn^{2+} ions that not only possess greater electron density than Mg^{2+}, even while occupying the same cation binding pockets, but also cause anomalous scattering of X-rays, a phenomenon that can be exploited for direct location of the ions in the electron density map.

To rule out the possibility that the presence of Mn^{2+} ions as a substitute for Mg^{2+} may alter the compact state of the RNA, we first characterized the effects of Mg^{2+}, Mn^{2+}, and Ca^{2+} on the compaction of the M-box using AUC and SHAPE. Results of both AUC and SHAPE experiments clearly show a fourfold greater affinity for the M-box binding to Mn^{2+} as compared to Ca^{2+} and Mg^{2+} in lower monovalent ion concentrations. This difference in affinity is, however, lost in the presence of 2.1 M monovalent ions. This observation confirms that along with a diffuse ionic atmosphere of loosely associated metal ions, which can be displaced by a higher concentration of monovalent ions, the M-box possesses a collection of specific cation binding sites, which are likely to play a critical role in gene regulation. Also, it confirms that

the extent of compaction is similar in the presence of all three metal ions tested. This, along with previous studies on the group I introns,[34,35,40] hammerhead ribozymes,[41] and other riboswitches,[33] suggest that Mn^{2+} ions could occupy Mg^{2+} sites in RNAs.

This is in fact what we observed in the Mn^{2+}-bound M-box structure. In addition to the six previously identified sites in the Mg^{2+}-bound M-box structure, two out of three sites predicted by phosphorothioate interference are also occupied by Mn^{2+}. Determination of the Mn^{2+}-bound M-box structure showed the presence of two molecules in the asymmetric unit of the crystal. Although this is exclusive to a particular crystal form and bears no physiological significance, the structural differences along with a difference in Mn^{2+} occupancies in the different cation sites of the two molecules allow us to make several interesting observations. For example, the difference between backbone arrangements in the P4 helix around metal core 2 and the presence of core 2 Mn^{2+} ions only in one chain suggest that modest perturbations in the structure, while maintaining the overall tertiary contacts, are still capable of affecting metal ion binding in the M-box. Therefore, core 2 sites (sites 5, 6, and 11) possibly represent regions of structural flexibility in the M-box, in contrast to our expectations for core 1. This is in agreement with previous phosphorothioate interference experiments where nucleotides constituting these sites 5 and 6 showed moderate to weak interferences at 0.5 mM Mg^{2+} and were not observed at 1 mM Mg^{2+}, implying that occupancy of these sites by metal ions could be bypassed under certain conditions.[32] Visualization of Mn^{2+} in the putative metal sites of core 3, which were previously only predicted by biochemical data, helps to establish them as divalent sites that may be important under cellular conditions. There are several explanations for why these sites could be visualized in the presence of Mn^{2+} but not of Mg^{2+}. It is possible that individual cation sites exhibit higher affinity for Mn^{2+} as compared to Mg^{2+}, leading to greater occupancy of these sites by Mn^{2+}. It is also possible that these sites are better visualized because of the higher resolution of diffraction data or because of the increased structural order in the neighboring P6 helix in the Mn^{2+}-bound structure.

One particular caveat in using crystallographic structures as a way to understand atomic level details of RNA–metal interactions is that inherent properties of a particular metal ion may influence subtle structural alterations in the RNA itself. However, the current structural analysis argues against this for the Mn^{2+}-chelated M-box structure, given that it can be superimposed with the Mg^{2+}-chelated M-box structure. We also observed a high degree of similarity for electrostatic surface potential comparisons between M-box RNAs bound to Mg^{2+} and Mn^{2+}, even for sites that were not occupied by a cation in the structural model. This could suggest that folding of the M-box is influenced by the formation of tertiary and long-range contacts potentially prior to cation binding.

Phylogenetic analysis of the distribution of M-box RNAs across bacterial genomes revealed that M-box riboswitches are most often employed for regulation of Mg^{2+} transporter genes.[22] However, at a lower frequency, M-box riboswitches appear to regulate expression of natural-resistance-associated macrophage protein genes, which typically function as transporters of Mn^{2+} or of iron. Although other explanations are possible, this observation raises the intriguing hypothesis that certain M-box riboswitches may function as sensors of Mn^{2+}, rather than Mg^{2+}. Given the higher concentration of Mg^{2+} within cells relative to Mn^{2+}, riboswitches that respond to Mn^{2+} would be likely to require specific Mn^{2+} cation binding sites. It is possible that subtle structural changes, such as positioning of an N7 group in relation to a Mn^{2+} ion, would be an efficient way to fine-tune M-box RNAs for sensing of metals other than Mg^{2+}. Such interactions may even conceptually resemble sites M10 and M12, which both include metal interactions to guanine N7 groups. Therefore, when considered together, our aggregate data on the structural analyses of Mg^{2+}-bound and Mn^{2+}-bound M-box aptamers have provided a structural basis for riboswitch-mediated sensing of divalent cations within the cellular context.

Materials and Methods

RNA preparation

For AUC and SHAPE reactions, DNA templates were amplified by PCR from *B. subtilis* IA40 chromosomal DNA (Bacillus Genetic Stock Center, Columbus, OH) using oligos SCB3 (5′ taatacgactcactatagggaacttcgttaggtg) and SCB4 (5′ ccttcaatcgtagagc). RNA was prepared by *in vitro* transcription for 2.5 h at 37 °C in 50-μl reactions. These reactions included: 30-pmol DNA template and buffer containing 30 mM Tris–HCl (pH 8.0), 10 mM DTT, 0.1% Triton X-100, 0.1 mM spermidine HCl, 5 mM each of nucleoside triphosphate (Roche), 40 mM $MgCl_2$, and ~50 μg/ml of recombinant T7 RNA polymerase. Reactions were terminated with loading dye containing 8 M urea. Following resolution on a urea denaturing 6% polyacrylamide gel, we cut the bands into ~1-mm cubes and incubated at 25 °C for 2.5 h in buffer containing 200 mM NaCl, 10 mM Tris–HCl (pH 7.5), and 10 mM ethylenediaminetetraacetic acid (pH 8.0). Eluted RNAs were then ethanol precipitated and resuspended in water.

SHAPE assays were performed with 1 pmol of RNA in 9-μl solutions containing 5 μl of 2× SHAPE buffer [10 mM Tris–HCl (pH 8.0) and 200 mM KCl] and 1 μl of 10× $MgCl_2$, $MnCl_2$, or $CaCl_2$. Experiments performed at high concentrations of monovalent ions included 4 M KCl in the 2× SHAPE buffer. Solutions were equilibrated for 2 h at 25 °C following which 1 μl of freshly prepared 65 mM NMIA solution was added. Samples were then incubated

for 45 min at 37 °C. Reactions were ethanol precipitated and resuspended in 11 μl of water with the 5′-^{32}P-labeled oligonucleotide SCB4 (5′ccttcaatcgtagagc). An extension reaction was then performed using Transcriptor Reverse Transcriptase (Roche), as described previously.[37] Samples were subjected to PAGE separation, and all polyacrylamide gels were visualized and quantified as described previously.[9]

AUC was performed essentially as described previously[9] using a Beckman AUC XL-I with absorbance optics. Sample (390 μl) and reference buffer were loaded into dual-sector charcoal-filled epon centerpieces. These were equilibrated to 20 °C for 1 h. Absorbance measurements at 260 nm were collected during centrifugation in an An60Ti rotor at 42,000 rpm for at least 4 h. Density and viscosity calculations for each buffer were made using SEDNTERP. Since no density and viscosity values for $MnCl_2$ are included in the SEDNTERP program, this buffer component was excluded from the analysis. Since $MnCl_2$ was present at sub-millimolar concentrations, data analysis was not significantly impacted by this exclusion. Divalent ions titrations were performed in buffer containing 10 mM Tris–HCl (pH 7.5) and 100 mM KCl. Data were analyzed using SedFit v9.4, assuming a partial specific volume (v_{bar}) of 0.53 cm^3/gm and a hydration value of 0.59 g/g in order to obtain the sedimentation coefficient. The sedimentation coefficient, R_H, a/b, and D were obtained from the analysis, and sedimentation coefficients were converted into $s_{20,w}$ by multiplying with the conversion factor obtained from the following equation:

$$\left(\eta_{T,b} / \eta_{20,w}\right) \times \left(\left(1 - \rho_{20,w}{*}\text{vbar}\right) / \left(1 - \rho_{T,b}{*}\text{vbar}\right)\right)$$

where $\eta_{T,b}$ is the viscosity of the buffer, $\eta_{20,w}$ is the viscosity of water at 20 °C, $\rho_{20,w}$ is the density of water at 20 °C, v_{bar} is the v_{bar} of the RNA at 20 °C, and $\rho_{T,b}$ is the density of the buffer.

To generate RNA for crystallization, we generated DNA templates by PCR using oligos WCW500 (5′gccagtgaattctaatacgactcactatagggcttcgttaggtgaggc) and AR004 (5′gctctagatggaagatcatgtgatttctc). The template for these reactions included the sequence of the *B. subtilis mgtE* M-box aptamer followed by an adenine nucleotide and the *glmS* ribozyme, as described previously.[9] Following phenol:chloroform extraction and ethanol precipitation of the PCR product, we set up *in vitro* T7 transcription reactions as described above. The resultant RNA products encompassed nucleotides 18–171 of the *B. subtilis mgtE* 5′ leader region and included three additional G:C base pairs at the terminus of the P1 helix. Immediately downstream of the aptamer was an unpaired adenine nucleotide and the *glmS* ribozyme.[9] Glucosamine-6-phosphate (2 mM) was supplied in the 10-ml transcription reactions to stimulate *glmS* self-cleavage and release of the M-box aptamer sequence.[9] Following extraction with phenol:chloroform: isoamylalcohol (25:24:1) and ethanol precipitation, we resuspended RNA in a gel-loading buffer containing 8 M urea and subjected it to denaturing PAGE on an 8% urea-polyacrylamide gel for 3.5 h. This resulted in a clear separation of the M-box RNA from the *glmS* RNA fragment. The band corresponding to the M-box RNA was excised, and the RNA was recovered by passive elution.[9] After ethanol precipitation, the RNA was resuspended in buffer [10 mM Hepes (pH 8.0) and 100 mM KCl] and dialyzed against 1000× volume of the same buffer for a minimum of 2 h with two buffer exchanges. Following dialysis, we concentrated the RNA to 4 mg/ml using YM-3 Microcon centrifugal filters.

Crystallization and X-ray data collection

Irregular crystals for the M-box RNA were obtained using hanging-drop vapor diffusion by mixing 1.0 μl of RNA with 0.9 μl of crystallization buffer [40 mM Hepes (pH 7.4), 20 mM KCl, 12 mM spermine·4 HCl and 10% methyl-2,4-pentanediol] and 0.1 μL of 0.1 mM $MnCl_2$ and by equilibrating against a reservoir solution consisting of 35% methyl-2,4-pentanediol. To obtain better quality crystals, we performed an optimization using an additive screen (Hampton Research), where 1.0 μl of RNA at 4 mg/ml was mixed with 0.8 μl of crystallization buffer, 0.1 μl of 0.1 M $MnCl_2$, and 0.1 μl of additive. Rod-shaped crystals were obtained in the presence of 50 mM ammonium sulfate as the additive. Crystals were picked from the crystallization drop and were directly flash frozen in liquid nitrogen. Diffraction data were collected at the Mn^{2+} absorption edge (6.547 keV) at beamline 19BM (Advanced Photon Source, Chicago), with the best crystal diffracting to 3 Å with cell dimensions $a=69.80$ Å, $b=103.30$ Å, $c=129.84$ Å, and $\alpha=\beta=\gamma=90°$. Another crystal from the same drop yielded higher-resolution data (1.86 Å), which was collected at 12.659 keV on beamline 19ID and showed cell dimensions $a=68.78$ Å, $b=102.49$ Å, $c=126.38$ Å, and $\alpha=\beta=\gamma=90°$. Data statistics are compiled in Table 1. M-box crystals from the same crystallization drop often displayed non-isomorphism. This phenomenon has been noted in the past for crystals of the P4–P6 domain of group I intron.[42]

Table 1. Data collection, refinement, and stereochemistry

	Mn^{2+} peak	Hires
Data collection		
Resolution (Å) (last shell)	50–2.90 (2.95–2.90)	50–1.86 (1.89–1.86)
Wavelength (Å)	1.89	0.98
Space group	$P2_12_12_1$	$P2_12_12_1$
Unit cell dimensions *a*, *b*, *c* (Å)	69.79, 103.29, 129.83	68.78, 102.48, 126.37
Unit cell angles α, β, γ (°)	90, 90, 90	90, 90, 90
I/σ (last shell)	23 (2.8)	25 (1.8)
R_{sym} (last shell)	0.12 (0.58)	0.09 (0.91)
Completeness (%) (last shell)	87 (72.8)	90.5 (69.9)
Redundancy (last shell)	5.0 (4.7)	5.7(5.6)
Refinement		
Resolution (Å)		47.4–1.86
No. of reflections		69,322
No. of working reflections		65,825
No. of free reflections (% total)		3497 (5%)
R_{work} (%)		19.2%
R_{free} (%)		22.8%
Structure and stereochemistry		
No. of atoms		
RNA		6863
Water		540
Manganese		25
Potassium		6
RMSD bond length (Å)		0.005
RMSD bond angles (°)		1.6

Structure determination

X-ray diffraction data were indexed, integrated, and scaled using HKL2000.[43] Molecular replacement was performed against the 2.9-Å data set using the Mg^{2+}-bound M-box structure [Protein Data Bank (PDB) 2QBZ] as a search model and using Phaser via the CCP4 suite.[44,45] The resulting solution showed good statistics with a *Z*-score of 46.2, an LLG of 3067, and *R*-factors of 23% and 29.7%. Using this solution as a search model, we performed molecular replacement against the 1.86-Å data set, yielding a solution with a *Z*-score of 46 and an LLG of 3491. Rigid-body refinement followed by simulated annealing was performed using phenix.refine.[46] Density corresponding to the P6 helix was visible at greater than 3 σ contour of the $F_o - F_c$ map, and this region was built manually using Coot.[47] Iterative model building using Coot along with refinement (phenix.refine) significantly reduced the crystallographic *R*-factor to 24% and R_{free} to 27%. Positive electron density in the $F_o - F_c$ map was used for the assignment of water molecules. Strong positive electron density in the $F_o - F_c$ map and distance and geometry constraints were used to place Mn^{2+} ions. Water molecules that displayed significantly lower *B*-factors as compared to the neighboring atoms were also an indication of occupancy by Mn^{2+}. An anomalous difference Fourier map created using sfall[45] was generated using the model and the 2.9-Å data collected at the Mn^{2+} edge. Positive anomalous peaks as strong as 21 σ were observed in this map and were used to further confirm the location of Mn^{2+} ions. The final model was refined to an *R*-factor of 19.2% and R_{free} of 22.8%. Refinement statistics are shown in Table 1. Electrostatic potential calculations were performed using PDB2PQR[48] (to prepare input files for APBS) and APBS,[49] and visualization was done using PyMOL. Illustrations were made using UCSF Chimera.[50]

Accession numbers

Coordinates and structure factors have been deposited in the PDB with accession number 3PDR.

Acknowledgements

Research on metal-responsive riboswitches in the Winkler laboratory is funded by the National Institutes of Health grant GM081882 with additional support from the Welch Foundation (I-1643) and The University of Texas Southwestern Medical Center Endowed Scholars Program.

References

1. Giedroc, D. P. & Arunkumar, A. I. (2007). Metal sensor proteins: nature's metalloregulated allosteric switches. *Dalton Trans.* 3107–3120.
2. O'Halloran, T. V. (1993). Transition metals in control of gene expression. *Science*, **261**, 715–725.
3. Ma, Z., Jacobsen, F. E. & Giedroc, D. P. (2009). Coordination chemistry of bacterial metal transport and sensing. *Chem. Rev.* **109**, 4644–4681.
4. Cayley, S., Lewis, B. A., Guttman, H. J. & Record, M. T., Jr (1991). Characterization of the cytoplasm of *Escherichia coli* K-12 as a function of external osmolarity. Implications for protein–DNA interactions *in vivo*. *J. Mol. Biol.* **222**, 281–300.
5. Froschauer, E. M., Kolisek, M., Dieterich, F., Schweigel, M. & Schweyen, R. J. (2004). Fluorescence measurements of free [Mg^{2+}] by use of mag-fura 2 in *Salmonella enterica*. *FEMS Microbiol. Lett.* **237**, 49–55.
6. Maguire, M. E. (2006). Magnesium transporters: properties, regulation and structure. *Front. Biosci.* **11**, 3149–3163.
7. Moomaw, A. S. & Maguire, M. E. (2008). The unique nature of Mg^{2+} channels. *Physiology (Bethesda)*, **23**, 275–285.
8. Cromie, M. J., Shi, Y., Latifi, T. & Groisman, E. A. (2006). An RNA sensor for intracellular Mg^{2+}. *Cell*, **125**, 71–84.
9. Dann, C. E., III, Wakeman, C. A., Sieling, C. L., Baker, S. C., Irnov, I. & Winkler, W. C. (2007). Structure and mechanism of a metal-sensing regulatory RNA. *Cell*, **130**, 878–892.
10. Draper, D. E., Grilley, D. & Soto, A. M. (2005). Ions and RNA folding. *Annu. Rev. Biophys. Biomol. Struct.* **34**, 221–243.
11. Woodson, S. A. (2005). Metal ions and RNA folding: a highly charged topic with a dynamic future. *Curr. Opin. Chem. Biol.* **9**, 104–109.
12. Sigel, R. K. (2007). Intimate relationships between metal ions and nucleic acids. *Angew. Chem., Int. Ed. Engl.* **46**, 654–656.
13. Draper, D. E. (2008). RNA folding: thermodynamic and molecular descriptions of the roles of ions. *Biophys. J.* **95**, 5489–5495.
14. Pyle, A. M. (2002). Metal ions in the structure and function of RNA. *J. Biol. Inorg. Chem.* **7**, 679–690.
15. Schwalbe, H., Buck, J., Furtig, B., Noeske, J. & Wohnert, J. (2007). Structures of RNA switches: insight into molecular recognition and tertiary structure. *Angew. Chem., Int. Ed. Engl.* **46**, 1212–1219.
16. Montange, R. K. & Batey, R. T. (2008). Riboswitches: emerging themes in RNA structure and function. *Annu. Rev. Biophys.* **37**, 117–133.
17. Dambach, M. D. & Winkler, W. C. (2009). Expanding roles for metabolite-sensing regulatory RNAs. *Curr. Opin. Microbiol.* **12**, 161–169.
18. Roth, A. & Breaker, R. R. (2009). The structural and functional diversity of metabolite-binding riboswitches. *Annu. Rev. Biochem.* **78**, 305–334.
19. Nudler, E. & Mironov, A. S. (2004). The riboswitch control of bacterial metabolism. *Trends Biochem. Sci.* **29**, 11–17.
20. Collins, J. A., Irnov, I., Baker, S. & Winkler, W. C. (2007). Mechanism of mRNA destabilization by the *glmS* ribozyme. *Genes Dev.* **21**, 3356–3368.
21. Barrick, J. E., Corbino, K. A., Winkler, W. C., Nahvi, A., Mandal, M., Collins, J. *et al.* (2004). New RNA motifs suggest an expanded scope for riboswitches in bacterial genetic control. *Proc. Natl Acad. Sci. USA*, **101**, 6421–6426.
22. Ramesh, A. & Winkler, W. C. (2010). Magnesium-sensing riboswitches in bacteria. *RNA Biol.* **7**, 77–83.

23. Lipfert, J., Das, R., Chu, V. B., Kudaravalli, M., Boyd, N., Herschlag, D. & Doniach, S. (2007). Structural transitions and thermodynamics of a glycine-dependent riboswitch from *Vibrio cholerae*. *J. Mol. Biol.* **365**, 1393–1406.
24. Baird, N. J. & Ferre-D'Amare, A. R. (2010). Idiosyncratically tuned switching behavior of riboswitch aptamer domains revealed by comparative small-angle X-ray scattering analysis. *RNA*, **16**, 598–609.
25. Kulshina, N., Baird, N. J. & Ferre-D'Amare, A. R. (2009). Recognition of the bacterial second messenger cyclic diguanylate by its cognate riboswitch. *Nat. Struct. Mol. Biol.* **16**, 1212–1217.
26. Groisman, E. A. (2001). The pleiotropic two-component regulatory system PhoP–PhoQ. *J. Bacteriol.* **183**, 1835–1842.
27. Alix, E. & Blanc-Potard, A. B. (2007). MgtC: a key player in intramacrophage survival. *Trends Microbiol.* **15**, 252–256.
28. Klein, D. J., Moore, P. B. & Steitz, T. A. (2004). The contribution of metal ions to the structural stability of the large ribosomal subunit. *RNA*, **10**, 1366–1379.
29. Christian, E. L. & Yarus, M. (1993). Metal coordination sites that contribute to structure and catalysis in the group I intron from *Tetrahymena*. *Biochemistry*, **32**, 4475–4480.
30. Forconi, M., Sengupta, R. N., Liu, M. C., Sartorelli, A. C., Piccirilli, J. A. & Herschlag, D. (2009). Structure and function converge to identify a hydrogen bond in a group I ribozyme active site. *Angew. Chem., Int. Ed. Engl.* **48**, 7171–7175.
31. Pecoraro, V. L., Hermes, J. D. & Cleland, W. W. (1984). Stability constants of Mg^{2+} and Cd^{2+} complexes of adenine nucleotides and thionucleotides and rate constants for formation and dissociation of MgATP and MgADP. *Biochemistry*, **23**, 5262–5271.
32. Wakeman, C. A., Ramesh, A. & Winkler, W. C. (2009). Multiple metal-binding cores are required for metalloregulation by M-box riboswitch RNAs. *J. Mol. Biol.* **392**, 723–735.
33. Serganov, A., Huang, L. & Patel, D. J. (2009). Coenzyme recognition and gene regulation by a flavin mononucleotide riboswitch. *Nature*, **458**, 233–237.
34. Juneau, K., Podell, E., Harrington, D. J. & Cech, T. R. (2001). Structural basis of the enhanced stability of a mutant ribozyme domain and a detailed view of RNA–solvent interactions. *Structure*, **9**, 221–231.
35. Cate, J. H., Hanna, R. L. & Doudna, J. A. (1997). A magnesium ion core at the heart of a ribozyme domain. *Nat. Struct. Biol.* **4**, 553–558.
36. Ennifar, E., Walter, P. & Dumas, P. (2003). A crystallographic study of the binding of 13 metal ions to two related RNA duplexes. *Nucleic Acids Res.* **31**, 2671–2682.
37. Merino, E. J., Wilkinson, K. A., Coughlan, J. L. & Weeks, K. M. (2005). RNA structure analysis at single nucleotide resolution by selective 2′-hydroxyl acylation and primer extension (SHAPE). *J. Am. Chem. Soc.* **127**, 4223–4231.
38. Garst, A. D., Heroux, A., Rambo, R. P. & Batey, R. T. (2008). Crystal structure of the lysine riboswitch regulatory mRNA element. *J. Biol. Chem.* **283**, 22347–22351.
39. Ali, M., Lipfert, J., Seifert, S., Herschlag, D. & Doniach, S. (2010). The ligand-free state of the TPP riboswitch: a partially folded RNA structure. *J. Mol. Biol.* **396**, 153–165.
40. Stahley, M. R., Adams, P. L., Wang, J. & Strobel, S. A. (2007). Structural metals in the group I intron: a ribozyme with a multiple metal ion core. *J. Mol. Biol.* **372**, 89–102.
41. Martick, M., Lee, T. S., York, D. M. & Scott, W. G. (2008). Solvent structure and hammerhead ribozyme catalysis. *Chem. Biol.* **15**, 332–342.
42. Cate, J. H. & Doudna, J. A. (2000). Solving large RNA structures by X-ray crystallography. *Methods Enzymol.* **317**, 169–180.
43. Otwinowsky, Z. & Minor, W. (1997). Processing of X-ray diffraction data collected in oscillation mode. *Methods Enzymol.* **276**, 307–326.
44. McCoy, A. J., Grosse-Kunstleve, R. W., Adams, P. D., Winn, M. D., Storoni, L. C. & Read, R. J. (2007). Phaser crystallographic software. *J. Appl. Crystallogr.* **40**, 658–674.
45. Collaborative Computational Project, Number 4. (1994). The CCP4 suite: programs for protein crystallography. *Acta Crystallogr., Sect. D: Biol. Crystallogr.* **50**, 760–763.
46. Adams, P. D., Gopal, K., Grosse-Kunstleve, R. W., Hung, L. W., Ioerger, T. R., McCoy, A. J. *et al.* (2004). Recent developments in the PHENIX software for automated crystallographic structure determination. *J. Synchrotron Radiat.* **11**, 53–55.
47. Emsley, P. & Cowtan, K. (2004). Coot: model-building tools for molecular graphics. *Acta Crystallogr., Sect. D: Biol. Crystallogr.* **60**, 2126–2132.
48. Dolinsky, T. J., Nielsen, J. E., McCammon, J. A. & Baker, N. A. (2004). PDB2PQR: an automated pipeline for the setup of Poisson–Boltzmann electrostatics calculations. *Nucleic Acids Res.* **32**, W665–W667.
49. Baker, N. A., Sept, D., Joseph, S., Holst, M. J. & McCammon, J. A. (2001). Electrostatics of nanosystems: application to microtubules and the ribosome. *Proc. Natl Acad. Sci. USA*, **98**, 10037–10041.
50. Pettersen, E. F., Goddard, T. D., Huang, C. C., Couch, G. S., Greenblatt, D. M., Meng, E. C. & Ferrin, T. E. (2004). UCSF Chimera—a visualization system for exploratory research and analysis. *J. Comput. Chem.* **25**, 1605–1612.